PHYSICAL REVIEW RESEARCH **4**, 023131 (2022)

Derivation of a governing rule in triboelectric charging and series from thermoelectricity

Eui-Cheol Shin,[1] Jae-Hyeon Ko,[2] Ho-Ki Lyeo,[3] and Yong-Hyun Kim[1,2,*]
[1] *Department of Physics, Korea Advanced Institute of Science and Technology (KAIST), Daejeon 34141, Republic of Korea*
[2] *Graduate School of Nanoscience and Technology, KAIST, Daejeon 34141, Republic of Korea*
[3] *Korea Research Institute of Standards and Science, Daejeon 34113, Republic of Korea*

(Received 3 May 2021; revised 31 December 2021; accepted 28 April 2022; published 17 May 2022)

Friction-driven static electrification is familiar and fundamental in daily life, industry, and technology, but its basics have long been unknown and have continually perplexed scientists from ancient Greece to the modern high-tech era. Despite its simple manifestation, triboelectric charging is believed to be very complex because of the unresolvable interfacial interaction between two rubbing materials. Here, we reveal a simple physics of triboelectric charging and triboelectric series based on friction-originated thermoelectric charging effects at the interface, characterized by the material density (ρ), specific heat (c), thermal conductivity (k), and Seebeck coefficient (S) of each material. We demonstrate that energy dissipational heat at the interface induces temperature variations in the materials and thus develops electrostatic potentials that will initiate thermoelectric charging across the interface. We find that the trends and quantities of triboelectric charging for various polymers, metals, semiconductors, and even lightning clouds are simply governed by the triboelectric factor $\xi = S/\sqrt{\rho c k}$. The triboelectric figure of merit is expressed with the triboelectric power $K = \xi\sqrt{t/\pi}$, of which the difference can be maximized up to $1.2\ \mathrm{V/W \cdot cm^{-2}}$ at the friction time $t = 1$ s. Our findings will bring significant opportunities for microscopic understanding and management of triboelectricity or static electrification.

DOI: 10.1103/PhysRevResearch.4.023131

I. INTRODUCTION

Triboelectric charging is mysterious because its fundamental origin has not been known for a long time [1–13]. The phenomenon itself is obvious, as in combing hair or lightning in daily life, and humanity discovered electricity from it and came to understand almost every aspect of electricity and magnetism through Maxwell's equations. But why do we not yet rigorously know which material is charged positively or negatively when two materials are rubbed in spite of the great success of quantum mechanics and condensed matter physics? What is the fundamental origin of the mysteriousness of triboelectric charging?

Here is a collection of even more puzzling facts about triboelectric charging, gleaned after thousands of years of observations:

(1) Triboelectric charging occurs universally. It occurs not only at solid-solid contacts, but also at various solid-liquid [14], solid-gas [15], liquid-liquid [16], and gas-gas [17] systems. Lateral friction dominantly induces a charging effect called triboelectrification [13], but normal contact also causes electrification to a large extent, in a process called contact electrification [5–8].

(2) Generally, triboelectric charging effects are negligibly small for metallic systems, but maximized for insulating polymeric systems [18].

(3) Triboelectric series do exist. Surprisingly, there is no consensus on the triboelectric series accepted by the community [19]. A general tendency was observed in the experiment, but reproducibility is not settled at the level of science. Middle-school textbooks have started to remove the triboelectric series from the contents [20], simply because it is not accurate enough.

(4) Even more peculiar triboelectric effects have been routinely observed; identical materials exhibit charging effects when rubbed together [1,21–23]; dust particles are charged depending on their size [24,25]; and groups of materials exhibit cyclic triboelectric charging [18,26].

To date, no single theory can satisfactorily explain this mysterious but fundamental phenomenon. The failure has been reluctantly attributed to the unknown complexity of interfacial interaction between two contacting materials [2,13]. Many researchers have proposed various scenarios for triboelectric charging, such as electron transfer due to work-function difference [3,4], direct ion or material transfer [6,7], thermionic emission [8], or triboemission [9], mechanochemistry [13], and flexoelectricity [10]. Each theory may explain a specific case or more, but its general application is very limited. With no general guiding principle, recent developments of the triboelectric-based energy harvesting technology [8,11,12] will be fundamentally hindered. Also, static electrification, which sometimes leads to fires at gas stations, lightning during air operations, and unintentional damage to electronic devices, is a growing worry for modern industry

---

[*] Corresponding author: yong.hyun.kim@kaist.ac.kr

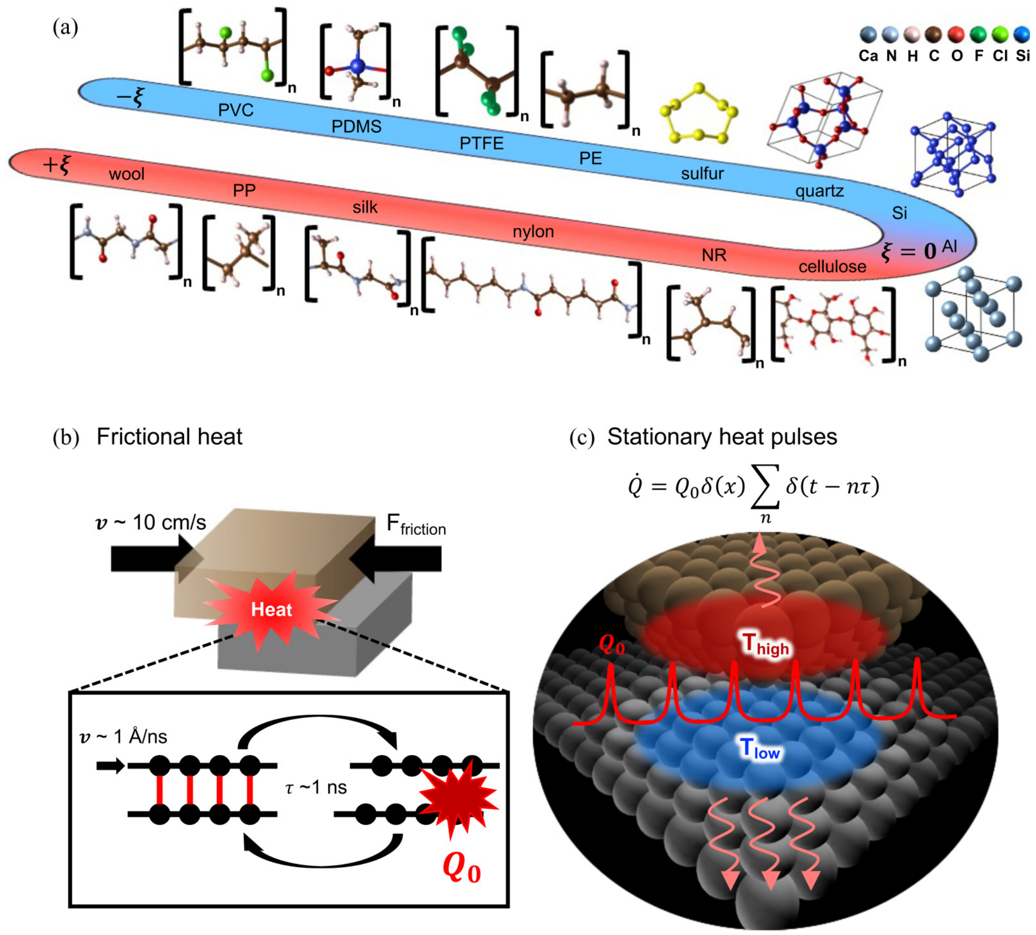

FIG. 1. Triboelectric series and frictional heat. (a) Triboelectric series quantified with triboelectric factor ξ for various triboelectric materials. The polymeric unit or crystal structure is also displayed. The triboelectric series has its origin at $\xi = 0$ for metals or superconductors for which the Seebeck coefficient is zero. (b) Frictional heat generated at the interface of two contacting materials. Microscopically, the frictional heat is associated with the bond-breaking process due to external mechanical motion. We assume that the relative speed of the two materials is 10 cm/s or 1 Å/ns, and the bond-breaking process repeats every $\tau = 1$ ns. (c) Stationary heat pulses $\dot{Q}(x,t) = Q_0\delta(x)\sum_n \delta(t-n\tau)$ located at the interface, representing frictional heat from successive bond-breaking processes. The temperature profile near the interface can be different with T_{high} and T_{low}, and there is an abrupt temperature drop across the interface depending on thermal properties of materials.

[27] and has to be controlled, if possible, via microscopic management.

Our goal here is to derive a simple governing rule of the mysterious triboelectric charging. To do this, we start with the assumption that a successful triboelectric theory should meet two conditions: (A) the triboelectric charging effect should follow a causality rule as other physics laws do; (B) the causality rule should be universally applicable. For example, the electron transfer due to work-function difference may explain contact electrification between metals, but this could happen without friction, violating condition (A). Thermionic emission could explain electron transfer when two solid materials contact at a strongly repulsive region, but this cannot happen at a gas-gas contact, violating condition (B).

The cause of the triboelectric charging effect is definitely friction between two contacting materials. Friction must be explicitly or implicitly connected to the electrification to satisfy condition (A). To make the cause more general to satisfy condition (B), we view the friction as *energy dissipation* regardless of its detailed complexity at the interface. This particularly makes sense at the first order for light frictional situations without severe damage or material transfer. Then, we know that the energy dissipation or frictional heat conduction at the interface between two materials results in temperature variations in the materials and an abrupt temperature drop at the interface [28]. We could naturally expect thermoelectric charge-redistribution effects according to the temperature profile [29–31]. Can this friction-originated thermoelectric charge redistribution be a solution to the mystery of triboelectric charging? At least, this scenario meets two conditions (A) and (B), as the thermoelectric effect is generally applicable in gases, liquids, and solids.

At the end, following the friction-originated thermoelectric charging scenario, we are able to rigorously quantify the triboelectric series, as shown in Fig. 1(a), by the triboelectric factor $\xi = S/\sqrt{\rho c k}$, which is expressed by the thermodynamic material properties such as the material density (ρ), specific heat (c), thermal conductivity (k), and Seebeck coefficient (S) of each material. Remarkably, the triboelectric series has an absolute origin at $S = 0$, and each material can be triboelectrically positive or negative depending on its Seebeck coefficient S. Based on our theory, the Seebeck coefficient S is the fundamental source of the mysteriousness of triboelectricity. Now we will demonstrate how the thermoelectric charging scenario leads to the unprecedented quantification of the triboelectric series.

II. FRICTIONAL HEAT GENERATION AND THERMOELECTRIC EFFECTS

When two materials are rubbed together, the mechanical energy dissipates into frictional heat. Microscopically, frictional heat is generated via a bond-breaking process at the interface, as schematically shown in Fig. 1(b). If the relative speed of the two contacting materials is about $v = 10\,\mathrm{cm/s}$, or $1\,\text{Å/ns}$, approximately $Q_0 = 0.01\,\mathrm{J/m^2}$ of heat is generated at the interface per $\tau = 1\,\mathrm{ns}$ (see Appendix A for estimation). To make the problem simple, we replace the frictional motion with a stationary heat source $\dot{Q}(x,t) = Q_0\delta(x)\sum_n^N \delta(t-n\tau)$ at the interface that generates successive N heat pulses, as shown in Fig. 1(c). Here, τ is the period of heat pulses, and t is the time for which friction applies. The δ-function-like heat pulse is a reasonable assumption because bond breaking and phonon excitation typically occur very quickly, on the time scale of subpicoseconds [32–34]. Also, the stationary heat generator model is naturally applicable to multiple contact electrification, in which similar bond-breaking energy dissipation occurs at the interface during the vertical contact-separation process but with a much larger time period τ of ms to seconds [23].

Generally, heat flows away from a heat source, and heat conduction is governed by Fourier's law, $\dot{Q} = -k\nabla T$. Here, $\dot{Q}$ is the heat density flux and ∇T is the temperature gradient. Once a temperature profile T is settled in a longer timescale, a thermo-electromotive force instantaneously develops due to the thermoelectric effect [31,35] according to $J = \sigma(E - S\nabla T)$, where J is the current density, σ is the electrical conductivity, and E is the electric field. At the steady state, the open-circuit condition $J = 0$ is applied throughout the materials. Then, the electrostatic potential V is simply described by

$$V = -ST, \tag{1}$$

since $E = -\nabla V$, and the accordingly redistributed charge density ρ_e is expressed as $\rho_e = \varepsilon S\nabla^2 T$ from Gauss' law, where ε is the dielectric constant. Therefore, if we can determine the temperature profile T from the heat conduction equation, we can obtain the electrostatic potential profile V and the charge density profile ρ_e with information of ε and S [31]. In this way, any thermal electrification between two contacting materials can be evaluated.

In a thermoelectric experiment with two contacting materials [31,36], heat flows from one material to the other. While temperature gradually varies within the materials, it suddenly drops at the interface. The abrupt interfacial temperature drop [28] is known to be determined by the interfacial thermal conductance κ. In our triboelectric model, the heat source is located at the interface of two materials, as schematically shown in Fig. S1 of the Supplemental Material (SM) [37]. Therefore, the interfacial temperature will be high, with a certain temperature difference between the two materials, and the temperatures will gradually decrease to the ambient temperature T_0. Figure S1 of the SM [37] also shows trivial linear solutions of temperature profiles of finite-size materials for thermoelectricity and triboelectricity at the steady state.

III. SEEBECK COEFFICIENT FROM QUANTUM MECHANICS

To proceed further, we need information about the Seebeck coefficient for various triboelectric materials. Unfortunately, Seebeck coefficients for triboelectric materials have not been well documented in experiments. This is partly because most triboelectric materials are not generally good conductors to measure Seebeck coefficients, or simply because we have not been interested in the property in this regard. In theory [31,38], however, the Seebeck coefficient is easily calculable from first-principles quantum mechanical calculations and sensitively depends on the location of the Fermi energy E_F and the local density of states at E_F. The location of E_F of a material is determined by various sample qualities and environment conditions and can readily vary even for a single material; for example, a fraction of charge will cause a wide swing of E_F for wide-gap insulating materials such as polymers. Because the E_F position for specific materials is also not known from experiments, we have to devise a way to locate E_F while considering general triboelectric environments. Our *ad hoc* choice is the universal alignment of the Fermi energy among various semiconductor materials and water [39]. As moisture is inevitable in the air to some extent, we take the $\mathrm{H_2/H^+}$ redox potential at -4.44 eV as the most probable location of E_F for various triboelectric materials.

With this choice, we quantum mechanically calculate the band alignment and Seebeck coefficient of representative triboelectric materials in Fig. 1(a)—wool (sulfur-crosslinked α-keratin), polypropylene (PP), silk, nylon, polyisoprene (NR: natural rubber), cellulose, Al, Si, quartz ($\mathrm{SiO_2}$), sulfur, polyethylene (PE), polytetrafluoroethylene (PTFE), polydimethylsiloxane (PDMS: silicone rubber), and polyvinyl chloride (PVC) [40–47]—using first-principles density-functional theory (DFT) formulation, as shown in Fig. 2 (see Appendix B for computational details). When the charge neutrality position E_neutral of a material is higher than the global Fermi energy E_F at -4.44 eV, the Seebeck coefficient becomes positive. Metallic Al has an almost zero Seebeck coefficient. Finally, when E_F is located above the E_neutral of a material, the Seebeck coefficient becomes negative. Generally, the magnitude of the Seebeck coefficient increases as the separation between E_F and E_neutral decreases [38].

In reality, the Fermi energy is not perfectly aligned and shows non-negligible variations depending on materials [39]. Also, the crystal structures that we used in DFT calculations do not represent real materials 100%. Therefore, we admit that our current Seebeck coefficients may contain appreciable errors in magnitude or sign. One relief is that the electronic structures of weakly interacting polymeric materials show no big changes depending on detailed crystal structures from first-principles DFT calculations [48]. With some tolerance in mind, it is still worthwhile to discuss, as a proof of concepts,

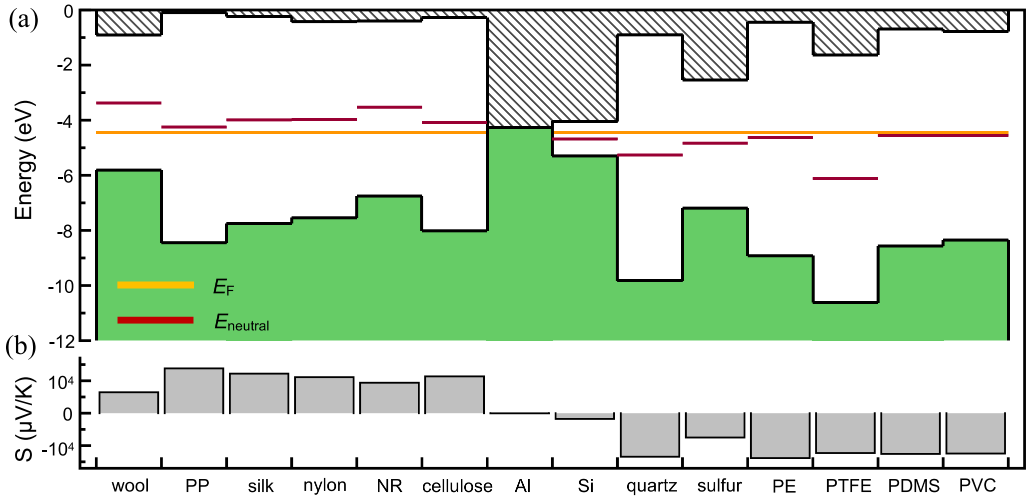

FIG. 2. Electronic structure and Seebeck coefficient of triboelectric materials. (a) Electronic structure of representative triboelectric materials (see text for full names) with the valence (filled) and conduction (half filled) bands from DFT calculations. The band offsets are aligned with reference to the vacuum level at zero energy, and the Fermi energy E_F is universally aligned with the hydrogen redox level at −4.44 eV. The charge-neutrality level for each material is marked as the neutral energy E_{neutral}. (b) DFT-calculated Seebeck coefficient S at assumed E_F for triboelectric materials.

thermoelectric charging and its tendency based on these *ad hoc* values, before any accurately measured value is available.

IV. HEAT PARTITION AND INTERFACIAL THERMAL CONDUCTANCE

To obtain the temperature profile of two *semi-infinite* materials in contact with an interfacial heat generator $\dot{Q}(x,t)$, we have to solve the one-dimensional heat equation, derived from Fourier's law [35],

$$\frac{\partial T}{\partial t} = \frac{k}{\rho c}\frac{\partial^2 T}{\partial x^2} + \frac{\dot{Q}}{\rho c}, \tag{2}$$

where $\alpha = k/\rho c$ is called thermal diffusivity. This equation is numerically solvable, but an analytical solution also exists with the help of two simplifications below.

Heat partition. When heat is generated from a bond-breaking process at an interface, the issue of how much the initial heat is partitioned into the two contacting materials 1 and 2 is nontrivial. As $Q = \rho c l T$, the initial heat needs to be partitioned depending on the volume (or the depth l) and $T = T_{\text{flash}} - T_0$, where T_{flash} is the instantaneously increased temperature [49]. We can think of two postulates of four different cases, as shown in Fig. 3, to determine $T_{1,2}$ that are necessary for solving the heat equation in Eq. (2). One postulate is that the flash temperatures are the same, $T_1 = T_2$, but with different depth l, i.e., (i) the first atomic layer, (ii) the phonon mean-free-path, or (iii) the thermal diffusion length of each material. The other postulate is that (iv) the heat is just partitioned by half to the depth of the phonon mean-free-path and the flash temperatures are not the same, $T_1 \neq T_2$. We have found that only the latter postulate (iv) provides separable triboelectric characteristics for each material (see Appendix C for details). The half-and-half postulate (iv) will be mainly used in our discussion for simplicity, but the other same-temperature postulate will provide similar physics but with a more complicated coupled formula, as displayed in Table S1 of the SM [37].

Interfacial thermal conductance. Depending on the interfacial thermal conductance κ, heat exchange occurs between two contacting materials, resulting in a change of the temperature difference, $\Delta T_{\text{int}} = T_1 - T_2$, at the interface. When κ is large (over 10 MW/m^2 K), ΔT_{int} is noticeably affected. But when κ is in the range 0.001–0.1 MW/m^2 K, the variation of ΔT_{int} is negligible, as shown in Fig. 4. So, we set $\kappa = 0$ as

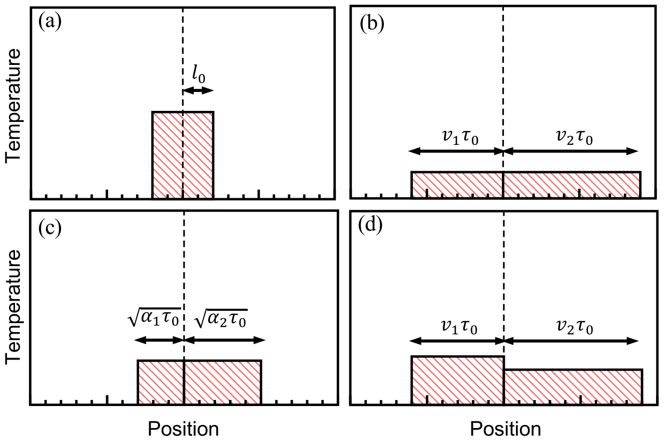

FIG. 3. Heat partition. Initial heat produced at the interface can be partitioned into two materials following four different schemes. (a) Partitioned heat is distributed within the first atomic layer l_0 with the same flash temperature. (b) Partitioned heat is distributed within the ballistic phonon mean-free-path $v\tau_0$ with the same flash temperature. v is the sound velocity and τ_0 is the short heating time of less than 0.1 ps. (c) Partitioned heat is distributed within the thermal diffusion length $\sqrt{\alpha\tau_0}$ with the same flash temperature. (d) Initial heat is partitioned by a half and distributed within the ballistic phonon mean-free-path $v\tau_0$. The flash temperatures are not the same.

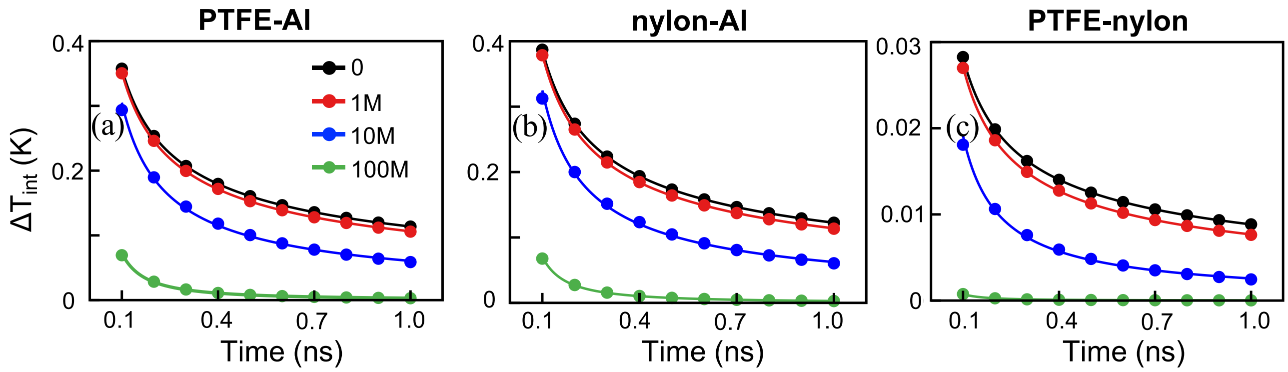

FIG. 4. Interfacial thermal conductance. (a)–(c) Evolution of temperature gap $\Delta T_{\rm int}$ at various values of interfacial thermal conductance κ from 0 to 100 $\mathrm{MW/m^2\,K}$, from numerical solutions for three representative triboelectric pairs (PTFE-Al, nylon-Al, and PTFE-nylon). When κ is less than 1 $\mathrm{MW/m^2\,K}$ in the weak-coupling regime, the change of $\Delta T_{\rm int}$ is insignificant, justifying the assumption $\kappa = 0$ used for analytic solutions.

a good approximation for triboelectric charging from weak interfacial couplings.

With these simplifications, we can separately and analytically obtain temperature profiles of individual materials.

V. TEMPERATURE PROFILES AND TRIBOELECTRIC CHARGING

To obtain temperature profiles, we solve Eq. (2) for three pairs of three prominent triboelectric materials; PTFE is known to be triboelectrically negative, and its $S < 0$; nylon is known to be positive and its $S > 0$; metallic Al is amphoteric and its S is nearly zero. We first numerically calculate temperature profiles while considering the nonzero interfacial thermal conductance κ and using experimental values for ρ, c, and k for three materials (see Appendix D for details). We then obtain the analytical solution using Green's functions when $\kappa = 0$,

$$\begin{aligned} T(x,t) &= \frac{1}{2}\frac{Q_0}{\sqrt{\pi\rho c k}}\sum_{n=0}^{N}\frac{e^{-x^2/4\alpha(t-n\tau)}}{\sqrt{t-n\tau}} \\ &\underset{t\gg\tau}{=} \frac{1}{2}\frac{\frac{Q_0}{\tau}}{\sqrt{\pi\rho c k}}\sqrt{t}\,\mathcal{E}_{3/2}\left[\frac{x^2}{4\alpha t}\right], \end{aligned} \qquad (3)$$

where x is the position from the interface (see Appendix E for the detailed derivation). The summation should be done up to $N < t/\tau$. When the summation is converted into the integral for large $t \gg \tau$, the special integral function $\mathcal{E}_m(z) = \int_1^\infty e^{-zu}/u^m du$ appears in the final form. Figure S2 of the SM [37] confirms that numerical solutions when $\kappa = 0$ match exactly the analytical solutions.

Figures 5(a)–5(c) show the evolution of the temperature profiles near the interface for three triboelectric pairs (PTFE-Al, nylon-Al, and PTFE-nylon) for a single heat pulse from Eq. (3) before the second pulse arrives. For a single heat pulse at the interface, the temperature profile exhibits a Gaussian shape with the dispersion of $2\sqrt{\alpha t}$. Due to their difference in thermal conductivity, PTFE and nylon stay at a relatively high temperature at the interface, whereas metallic Al cools down quickly. Because of this, we see noticeable temperature gaps for PTFE-Al and nylon-Al pairs and a small gap for the polymer pair. In our numerical solutions for all three pairs, as shown in Fig. 4, the temperature gap $\Delta T_{\rm int}$ is reduced slightly ($\sim$10%) when the interfacial thermal conductance κ is 1 $\mathrm{MW/m^2\,K}$.

With the temperature profiles and the Seebeck coefficients, we calculate the electrostatic potential profiles from Eq. (1) and the charge density distributions from $\rho_e = \varepsilon S \nabla^2 T$, as displayed in Figs. 5(d)–5(f) and 5(g)–5(i), respectively. We see that the polarity of S determines the polarity of V and ρ_e. Note that the open-circuit condition $J = 0$ is used in our derivation. This means that we do not allow any charge transfer across the interface, even though there is a potential difference between two contacting materials. In this adiabatic condition, the net charge of each material should be zero. When we allow charge transfer by shorting two materials at the interface, as happens in reality, a net charge will move across the interface following the electrostatic potential difference. For the PTFE-Al pair in Fig. 5(d), a net charge will move from high-potential PTFE to low-potential Al, completing the triboelectric charging effect; PTFE becomes negative and Al becomes positive. On the other hand, Al will be negatively charged for the nylon-Al pair. This reproduces the general experimental triboelectric tendency of the PTFE-Al-nylon series. The PTFE-nylon pair will show greater charge transfer because of the larger potential difference, in spite of the small temperature gap.

When more heat pulses in Eq. (3) are considered for a longer time, the temperature profile becomes non-Gaussian in shape (see Fig. S3 [37]). Figures 6(a)–6(c) show that, when N or t increases, the temperature profile spreads to μm with gradually increasing T at the interface. Figures 6(d)–6(f) and 6(g)–6(i) show corresponding voltage profiles and charge density distributions, respectively, for the three triboelectric pairs for large N up to 1000, corresponding to 1 μs. As t increases, charge is accumulated in the range of $\sim$30 nm from the interface and grows like a δ function. The additional charge accumulation or depletion for triboelectric insulators can be understood in terms of band bending effects due to the thermoelectromotive force $S\nabla T$ along the temperature gradient ∇T.

If we integrate the same charge near the interface for various t, the surface charge converges to a constant value after several ms, as shown in Fig. 7. Ultimately, the constant surface

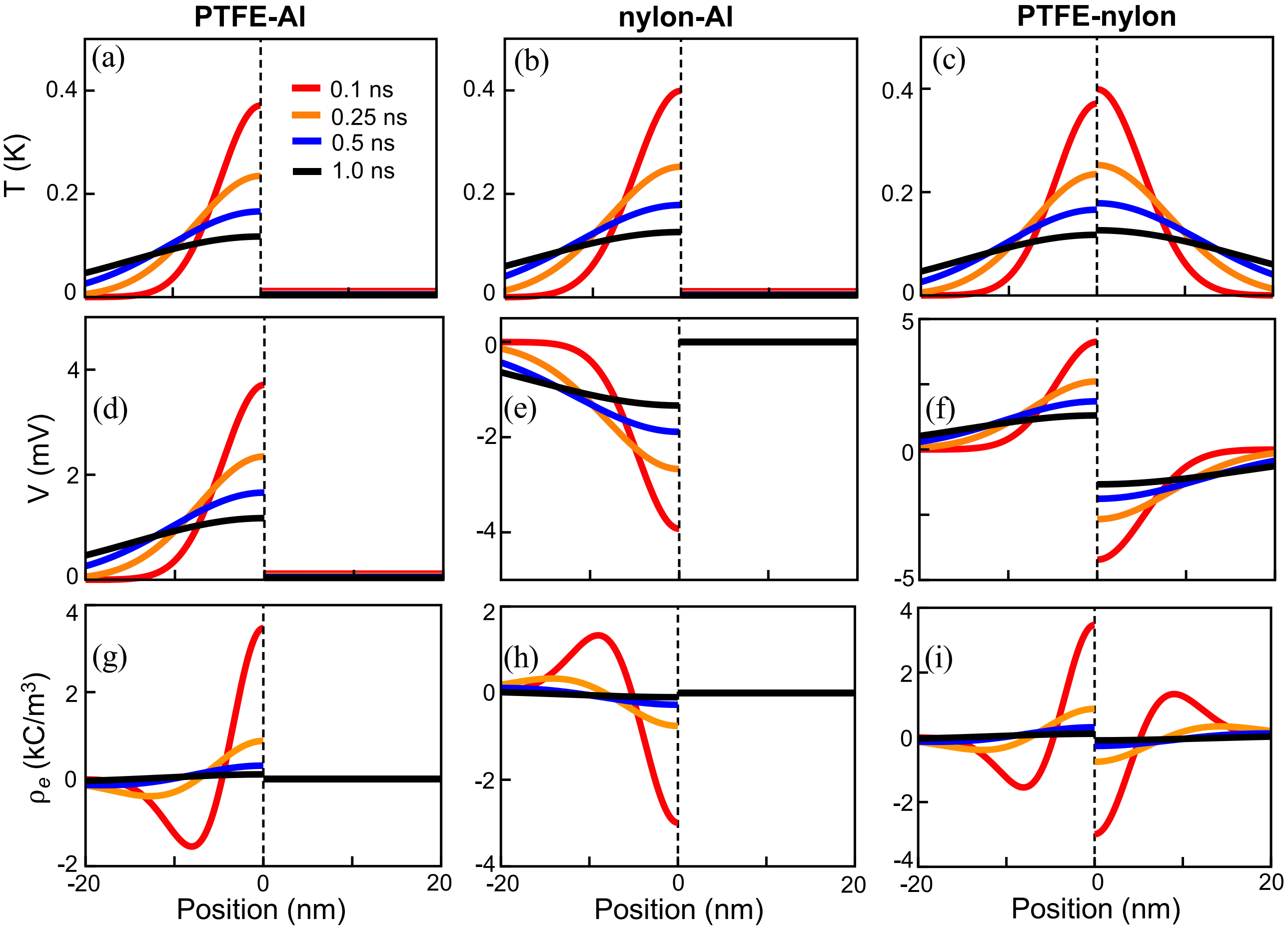

FIG. 5. Triboelectricity for a single heat pulse. (a)–(c) Evolution of temperature profiles after a single heat pulse at the interface for three representative triboelectric pairs (PTFE-Al, nylon-Al, and PTFE-nylon). The analytical solution in Eq. (3) is used for the plot. An abrupt temperature gap occurs at the interface. (d)–(f) Evolution of voltage profiles after a single heat pulse at the interface. We simply used Eq. (1) by multiplying $-S$ to $T(x,t)$. (g)–(i) Evolution of charge density profiles for the three triboelectric pairs. The charge density profile was obtained using $\rho_e = \varepsilon S \nabla^2 T$ with theoretical Seebeck coefficient S and dielectric constant ε.

charge density is evaluated as

$$\sigma_{\text{surface}} = -\frac{\varepsilon S}{2k}\frac{Q_0}{\tau}, \tag{4}$$

which is localized at the interface (see Appendix F for the detailed derivation). The δ-accumulated surface charge σ_{surface} is a kind of reservoir for triboelectric charging, ready to move across the interface when the short circuit is allowed. The monotonic increase of surface charge density is corroborated to a certain extent by experimental observation of surface charge increase in multiple-contact electrifications [23,50]. The magnitude of σ_{surface} is comparable to the experimental values [50] of $\sim 3\ \mu\text{C/m}^2$ although it is an adiabatic quantity with the opposite polarity.

VI. QUANTITATIVE TRIBOELECTRIC SERIES

Now we realize that triboelectric charging is solely determined by the potential difference at the interface $x = 0$ of two contacting materials, i.e., $V_1 - V_2 = S_2 T_2(0,t) - S_1 T_1(0,t)$. Note that this equation is typically used for evaluating a thermocouple [35] that measures the open-circuit voltage of a hot spot (see Fig. S4 [37]). Indeed, our triboelectric model is equivalent to a thermocouple. Because $\mathcal{E}_m(0) = 1/(m-1)$ when $m > 1$, we obtain the potential difference from Eq. (3) as

$$V_1 - V_2 = \frac{Q_0}{\tau}\sqrt{t/\pi}\left[\frac{S_2}{\sqrt{\rho_2 c_2 k_2}} - \frac{S_1}{\sqrt{\rho_1 c_1 k_1}}\right]. \tag{5}$$

This indicates that triboelectric charging is, remarkably, determined by the material characteristics S, ρ, c, and k of each material. We also find that the potential difference or triboelectric charging increases with the $\sqrt{t}$ dependency as the friction application time t increases.

Considering the polarity of triboelectric charging after the short-circuit condition in Eq. (5), we define a triboelectric factor ξ that rigorously quantifies the triboelectric series as

$$\xi = \frac{S}{\sqrt{\rho c k}}, \tag{6}$$

where the Seebeck coefficient S determines the absolute zero and sign of the triboelectric factor of a material. We suggest that the triboelectric series based on the triboelectric factor ξ is more fundamental than the transferred charge based quantification in Eq. (4) or experiments [11,12]. In

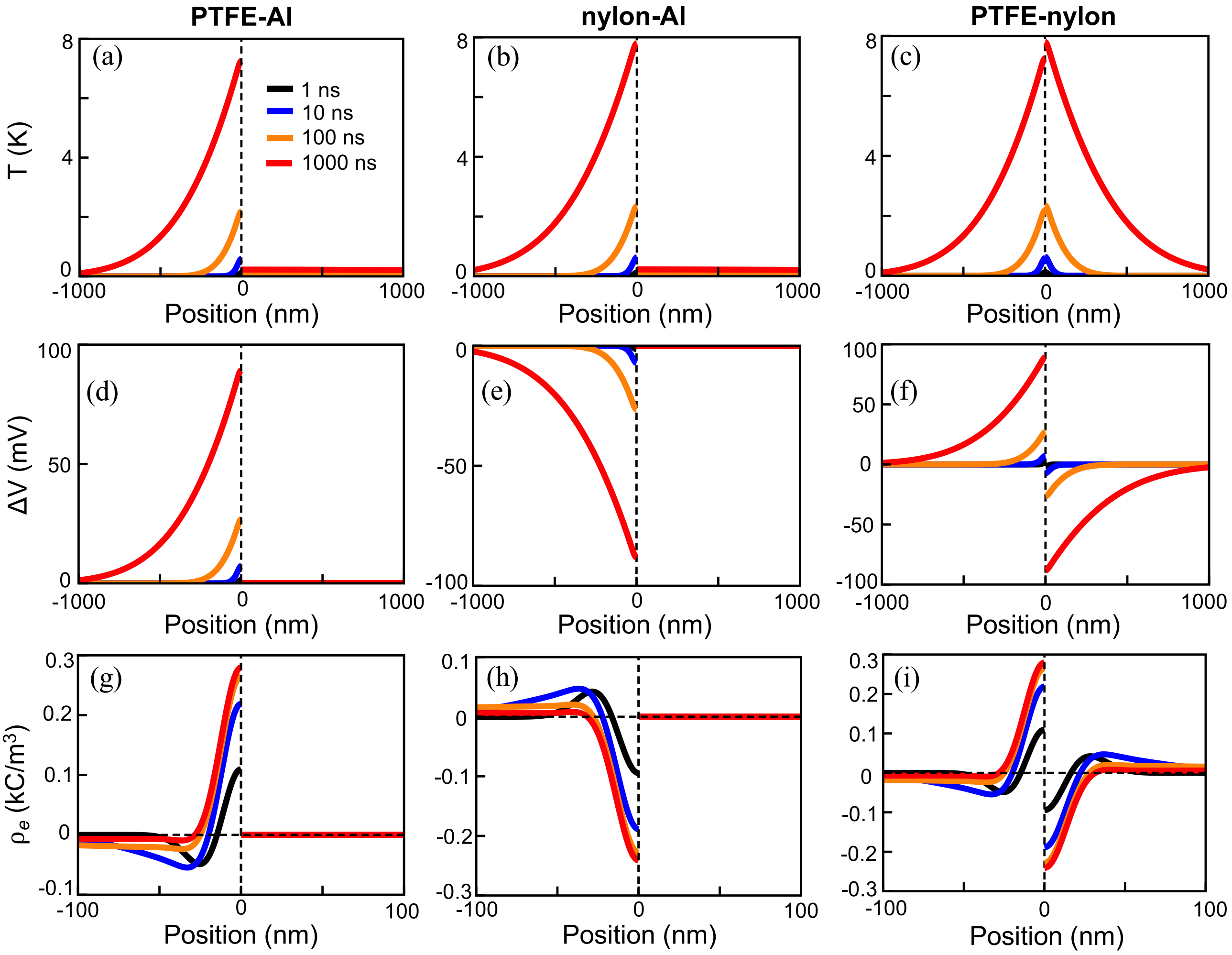

FIG. 6. Time evolution of triboelectricity. (a)–(c) Evolution of temperature profiles for multiple heat pulses up to 1000 for three representative triboelectric pairs (PTFE-Al, nylon-Al, and PTFE-nylon). (d)–(f) Evolution of electrostatic potential or voltage profiles ΔV at the interface for the three triboelectric pairs. The voltage profile quickly spreads to the depth of 1 μm within a few μs, and the interfacial voltage difference becomes appreciable. (g)–(i) Evolution of charge density profiles ρ_e up to 1 μs for the three triboelectric pairs. Localized positive charge accumulates within 30 nm of the interface for PTFE as time increases; negative charge accumulates for nylon. Note that the current flow is not allowed to cross the interface because of the open-circuit condition $J = 0$ that we used.

other words, triboelectric series should be defined by the direction, but not by the amount of charge transfer due to friction.

Following Eq. (6), we display the triboelectric series of the representative materials in Fig. 8(a) using theoretical S and experimental ρ, c, and k values (see Appendix G). Note that

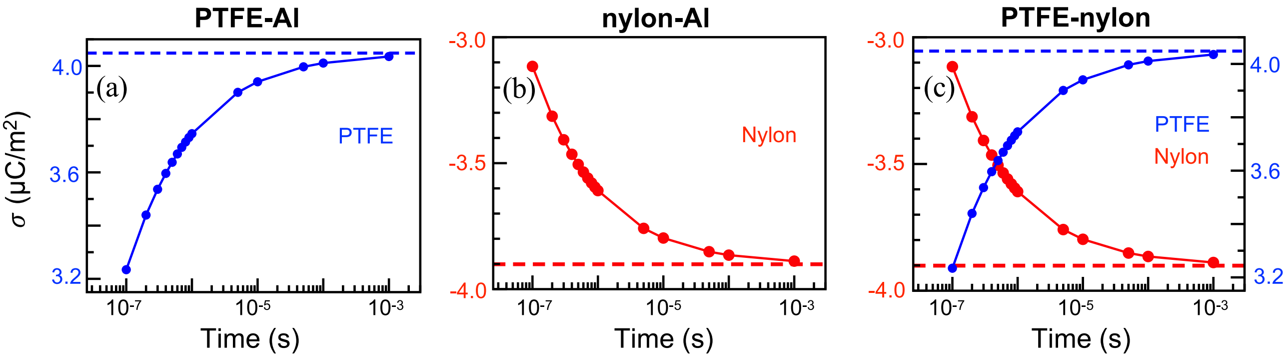

FIG. 7. Constant surface charge density. (a)–(c) Evolution of surface charge densities up to 1 ms for three representative triboelectric pairs (PTFE-Al, nylon-Al, and PTFE-nylon). The surface charge density σ_{surface} is obtained by integrating only the localized interfacial charge with the same polarity in Figs. 6(g)–6(i). σ_{surface} converges to a constant value. Al's surface charge density is negligible (not shown).

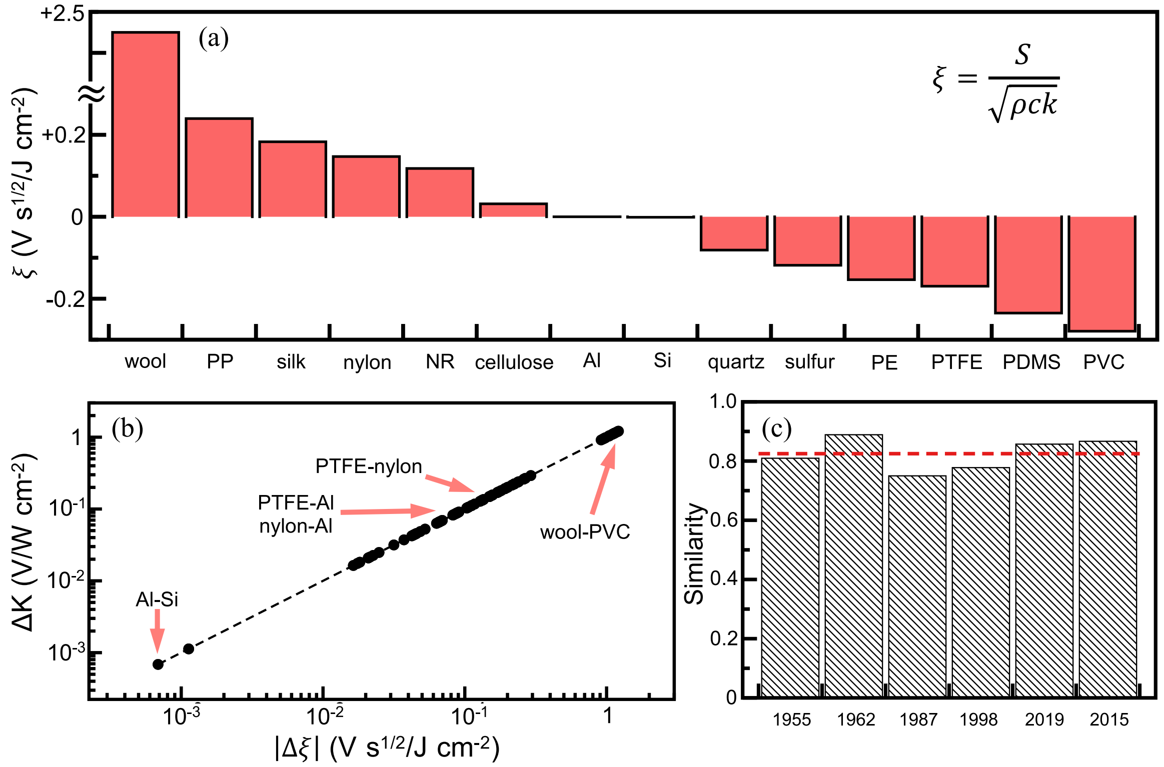

FIG. 8. Quantitative triboelectric series and figure of merit. (a) Triboelectric series quantified by triboelectric factor $\xi = S/\sqrt{\rho c k}$. The Seebeck coefficient determines the sign and zero of the triboelectric series. Polymeric materials have large ξ values because of large S and low ρ (density) and k (thermal conductivity). (b) Triboelectric figure of merit quantified by the triboelectric power difference $\Delta K = \Delta\xi\sqrt{t/\pi}$ for various triboelectric pairs at $t = 1$ s. The wool-PVC pair shows the largest ΔK of 1.2 V/W cm^{-2}. (c) The similarity of various triboelectric series in the literature (Table I) with respect to the quantitative triboelectric series of the present study. The average similarity is about 83%.

ξ is large for small ρ and k, e.g., as in polymeric materials. It may be possible to obtain more accurate triboelectric series for well-characterized material samples, particularly with carefully measured values of S and k. One interesting thing about the new quantity ξ is its unit V s$^{1/2}$/J cm^{-2}, which may be associated with electrostatic potential per unit energy density, but not exactly because of s$^{1/2}$.

The charge is not yet transferred in our current derivation of triboelectric charging. Therefore, it is awkward to define the efficiency of triboelectricity. Still, we can use Eq. (5) to evaluate the strength of triboelectric charging. We propose triboelectric power K as a new figure of merit of triboelectricity,

$$K = \xi\sqrt{t/\pi}, \tag{7}$$

of which the unit is V/Wcm^{-2}, representing the electrostatic potential per unit power density. Then, we obtain triboelectric voltage $\Delta V = \Delta K\frac{Q_0}{\tau}$, which is analogous to the thermoelectric formula $\Delta V = S\Delta T$ with the thermoelectric power S in the unit of V/K, representing the electrostatic potential per unit temperature. The triboelectric power K becomes more significant with the $\sqrt{t}$ dependency when the friction time t increases. In Fig. 8(b), we plot the triboelectric power difference ΔK for various triboelectric pairs for $t = 1$ s, reaching 1.2 V/W cm^{-2} for the wool-PVC pair.

To check the reliability of our quantitative triboelectric series, we compare similarity between various triboelectric series (see Appendix H for details), as shown in Fig. 8(c). We found that our quantitative triboelectric series is on average about 83% similar to other experimental triboelectric series reported in the literature [11,12,20,51–54], as listed in Table I. We can clearly recognize a general order of nylon, cellulose, and PTFE. While the order of wool, silk, and nylon is not settled in the series, we know that their ξ values can be sensitively modified with detailed values of S, ρ, c, and k. The remarkable similarity reflects that, in spite of various levels of approximations in our triboelectric theory, the thermoelectric charging scenario quite reasonably captures the essence of what happens in triboelectricity. Now we cautiously claim that the unsolved mystery of triboelectric charging can be attributed to the sensitive sample-by-sample dependency of the ξ value or S. This may make sense particularly for polymeric insulators, for which the Fermi energy and thus S can be sensitively altered by sample quality and environment.

VII. LIGHTNING CLOUDS

To demonstrate the general applicability of our heat-based triboelectric theory to nonsolid systems, we apply the theory to the problem of triboelectric charging in lightning clouds. The physical quantities S, ρ, c, and k could be well defined in theory for gases and liquids, although the thermoelectricity of gases and liquids might be more complicated [55]. Assuming a rigid contact between two clouds, we can roughly estimate the behavior of triboelectric charging in lightning clouds, as shown in Figs. 9(a) and 9(b). For simplicity, we treat the

TABLE I. Triboelectric series reported in the literature [11,12,20,51–54] and the present study for representative triboelectric materials including wool, polypropylene (PP), silk, nylon, polyisoprene (NR: natural rubber), cellulose, Al, Si, quartz (c-SiO$_2$), sulfur, polyethylene (PE), polytetrafluoroethylene (PTFE), polydimethylsiloxane (PDMS: silicone rubber), and polyvinyl chloride (PVC). Despite some ambiguity in the experimental materials, we consider fur, hair, and wool as sulfur-crosslinked α-keratin, cotton and wood as cellulose, and rubber as silicone rubber. The triboelectric series in the middle-school text [20] has been removed in the recent edition.

Most positive ————————————————————▶ Most negative	Pub. year
wool → **nylon** → **cotton** → silk → PVC → PE → **PTFE**	1955 [51]
nylon → wool → silk → **cotton** → NR → S → PE → PVC → **PTFE**	1962 [52]
nylon → wool → silk → paper → **cotton** → PE → PP → PVC → Si → **PTFE**	1987 [53]
quartz → **nylon** → wool → silk → **cotton** → paper → metals → rubber → **PTFE** → PVC	1998 [54]
Copy paper → **nylon** → PP → quartz → PE → PDMS → **PTFE** → PVC	2019 [11,12]
fur → glass → silk → wood → rubber → plastic	2015 [20]
wool → PP → silk → **nylon**→ NR → **cellulose** → Al → Si → quartz → S → PE → **PTFE** → PDMS → PVC	2022[present]

air as an ideal gas, following $pV = (\frac{m}{M})RT$ or $p = \rho RT/M$, where p is the pressure, V is the volume, m is the mass, M is the mass of 1-mole air, and R the gas constant. We also assume that two airs have different base temperatures T_1 and T_2, but nearly the same pressure p and the same Seebeck coefficient S. The thermal conductivity of an ideal gas has a temperature dependency of $k \sim \sqrt{T}$. As ρc is proportional to $1/T$, ρck is proportional to $1/\sqrt{T}$. Then, the triboelectric power difference of the two frictional airs can be written as

$$\Delta K = K_1 - K_2 = \frac{S\sqrt{t/\pi}}{\sqrt{\rho_1 c_1 k_1}}\left[1 - \left(\frac{T_2}{T_1}\right)^{1/4}\right], \qquad (8)$$

which indicates that ΔK is positive if T_2/T_1 is less than 1. The triboelectric factor $\xi = S/\sqrt{\rho ck}$ of air is $20.4\,\mathrm{V\,s^{1/2}/J\,cm^{-2}}$, which is much larger than those of typical triboelectric materials in Fig. 8(a). Once the triboelectric potential difference is developed following Eq. (8), various charge carriers may directly move across the interface of lightning clouds. Figures 9(a) and 9(c) show that the rising higher-temperature air is triboelectrically positively charged, and the lower-temperature air is negatively charged [17].

VIII. DISCUSSION

The triboelectric nanogenerator (TENG) [8,11,12] has been around for about a decade as a plausible energy harvesting technology from various mechanical energy sources. The technology is believed to be very close to commercialization. Although there have been many engineering attempts to improve its device design for better efficiency, there was no specific guiding rule for material selection. Our quantitative theory clearly suggests how to select triboelectric materials and how to control individual properties to achieve high triboelectric figures of merit. The theory can also be used for minimizing static electrification and preventing lightning damage.

New quantities for triboelectric charging, i.e., the triboelectric factor ξ and the triboelectric power K in Eqs. (6) and (7), can serve as a golden rule for understanding and microscopic management of static electrification. For example, to maximize triboelectric charging for energy harvesting, one needs to design sparse or porous materials with large Seebeck coefficients, small material densities ρ, and small thermal conductivities k. Generally, organic polymer materials possess these properties. It is also desirable to maximize $\Delta\xi$ such that the Seebeck coefficient can be induced to have opposite polarity by intentional or unintentional doping. This may be readily achievable in inorganic semiconductor materials. To this end, organic-inorganic hybrid materials such as colloidal quantum-dot solids could be a good candidate. Finally, the

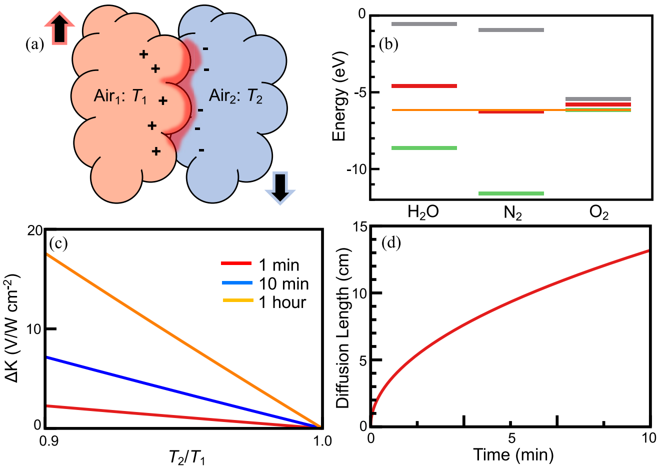

FIG. 9. Triboelectricity in lightning clouds. (a) Schematic of two frictional airs with different temperatures T_1 and T_2 in lightning clouds. We found that the higher-temperature rising air is positively charged, and the lower-temperature sinking air is negatively charged. (b) DFT-aligned molecular orbitals (MO) of H$_2$O, N$_2$, and O$_2$ in air. The highest occupied molecular orbital (HOMO) and the lowest unoccupied molecular orbital (LUMO) are marked by green and grey solid lines, respectively. The Fermi energy and the charge neutrality position are marked by orange and red solid lines, respectively. Because O$_2$ takes electrons easily from the environment, we set the Fermi energy to the HOMO of O$_2$. The Seebeck coefficient of air was calculated to be 0.01 V/K for H$_2$O molecules. (c) Triboelectric power difference $\Delta K = K_1 - K_2$ of two frictional airs depending on the ratio of temperatures at $t = 1$ min, 10 min, and 1 h. The positive value indicates that the higher-temperature air is charged positively. (d) Thermal diffusion length $2\sqrt{\alpha t}$ of the interfacial temperature profile of lightning airs as a function of frictional time t. For this estimation, we used $= 1.25\,\mathrm{kg/m^3}$, $c = 736\,\mathrm{J/kg\,K}$, and $k = 0.026\,\mathrm{W/m\,K}$ [56]. The exponential temperature distribution spreads up to 13 cm at $t = 10$ min.

unique power-law dependency of $\sqrt{t}$ implies that a longer friction time is limitedly better for energy harvesting.

IX. CONCLUSION

We rigorously proved that simple thermoelectric physics exists in triboelectric charging and the triboelectric series, which have been unsolved for a long time. Friction-originated thermoelectric charging is a key to quantitatively understanding the fundamental phenomenon. After the unprecedented quantification $\xi = S/\sqrt{\rho c k}$ of triboelectric series materials, we can now see why static electrification occurs significantly for polymeric insulating materials and negligibly for metallic materials. Our findings will pave the way to solving various mysteries of triboelectric charging and offer significant opportunities for controlling static electrification at the microscopic level.

All data are available in the main text or the Supplemental Material [37], or through the corresponding author upon reasonable request.

ACKNOWLEDGMENTS

We thank H.-H. Nahm, J. Y. Park, S.-Y. Kim, S. Jeong, and J. Kang for discussion. This work was supported by National Research Foundation of Korea (NRF) Grants No. 2016R1A5A1008184, No. 2019R1A6A1A10073887, and No. 2019M3D1A1078302 and by the Grand Challenge 30 program from the College of Natural Sciences, KAIST.

Y.-H.K. conceived the idea and designed the research. E.-C.S. and Y.-H.K. developed the theory, performed the calculations, and wrote the manuscript. J.-H.K. contributed to the early stage of the research. H.-K.L. contributed to the interpretation of the research. All authors commented on the manuscript.

Y.-H.K. and E.-C.S. have a patent application (KR-10-2021-0000860, 10-2021-0049278, pending in the Republic of Korea), which disclose methods for designing and evaluating triboelectric materials and energy harvesters.

APPENDIX A: ROUGH ESTIMATION OF FRICTIONAL HEAT

We assume a relative speed v of 10 cm/s or 1 Å/ns for the two rubbing materials. The typical magnitude of van der Waals (vdW) interactions E_{vdW} is on the order of 1 KJ/mol [57]. We can think of an energy density of about E_{vdW}/A for a one-to-one vdW bond of an ideal square lattice with a lattice constant of 1 Å, where A is the contact area defined by 1 Å^2. As a result, vdW energy between the two materials is approximately 10 meV/Å^2, as shown in Fig. S5 of the SM [37]. This estimated value can be justified by first-principles DFT calculations. Table S2 of the SM [37] shows the vdW binding energy E_{b} per contact area for several systems (Fig. S6 [37]). For both the polymer-polymer and the metal-polymer contacts, we obtain an order of 10 meV/Å^2, consistent with the above estimation for the ideal square lattice. Then, mechanical energy is supplied to break the vdW bonding, and only a fraction of the bond-breaking energy may be converted into the frictional heat Q. The fraction may be associated with the friction coefficient μ, which is assumed to be 0.1. Then, the heat generation rate is roughly estimated to be $Q_0 = 0.01\ \mathrm{J/m^2}$ per $\tau = 1$ ns. We used this value for numerical estimations. Frictional heat can be generated continuously or in the form of pulses.

APPENDIX B: DFT CALCULATION OF SEEBECK COEFFICIENTS

To obtain theoretical Seebeck coefficients, we performed first-principles DFT calculations using the Vienna *ab initio* simulation program (VASP) with projector-augmented wave (PAW) pseudopotentials in the VASP database [58] and the Perdew-Burke-Ernzerhof (PBE) functional [59] for various triboelectric materials, for which crystal structures are known from experiments, as displayed in Figs. S7–S10 [37]. To correct the underestimated DFT band gaps, we used the Heyd-Scuseria-Ernzerhof (HSE06) exchange-correlation functional [60] with mixing parameters from the reciprocal of the macroscopic dielectric constant $1/\varepsilon^{\infty}_{\mathrm{PBE}}$ [61] and a screening parameter of 0.2 Å^{-1}. The mixing parameters based on $\varepsilon^{\infty}_{\mathrm{PBE}}$ provide the significantly reduced error for large band gap systems such as polymeric materials. The macroscopic dielectric constant was calculated within the random phase approximation scheme using PBE wave functions, as listed in Table S3 [37]. This dielectric constant was also used for calculating the charge-density distribution. Band alignment was done using multilayer slab models and their vacuum potentials defined by the Hartree potential [62], which is commonly shared in PBE and HSE06 calculations.

The kinetic energy cutoff of 500 eV was used for all calculations. All materials were relaxed until the Hellman-Feynman atomic forces were less than 0.03 eV/Å. The linear tetrahedron method was used for the Brillouin-zone sampling with the following grid: (4×2×2) for α-keratin; (4×1×4) for polypropylene (PP); (4×4×4) for silk (fibroin); (2×4×4) for nylon; (4×2×2) for polyisoprene (NR); (4×2×2) for cellulose; (12×12×12) for Al; (4×4×4) for Si; (4×4×4) for quartz ($\mathrm{SiO_2}$); (4×4×2) for sulfur; (4×2×2) for polyethylene (PE); (4×2×2) for polytetrafluoroethylene (PTFE); (4×2×4) for polydimethylsiloxane (PDMS) and polyvinyl chloride (PVC).

The Seebeck coefficient was calculated [38] at the universally aligned Fermi energy E_{F} using

$$S(E_{\mathrm{F}}) = -\frac{1}{eT_0}\frac{\int N(E)(E-E_{\mathrm{F}})\left(-\frac{df}{dE}\right)dE}{\int N(E)\left(-\frac{df}{dE}\right)dE}, \tag{B1}$$

where e is the electron charge, T_0 is the ambient temperature (300 K), $N(E)$ is the DFT density of states of each material, and f is the Fermi-Dirac distribution function. In general, S is positive if E_{F} is lower than the charge-neutrality energy E_{neutral}, and vice versa. $S = 0$ if $E_{\mathrm{F}} = E_{\mathrm{neutral}}$.

It may be crucial to check whether theoretical Seebeck coefficients from Eq. (B1) properly represent experimental values at least in orders of magnitude. Therefore, we compared the experimentally well-documented Seebeck coefficients of Al and Si with DFT-based theoretical values. The experimental Seebeck coefficient of Al is $-1.8\ \mu$V/K [63], while the calculated one is $-2.5\ \mu$V/K at 300 K. For Si, the experimental Seebeck coefficient is $-673\ \mu\text{V/K}$ [64], very close to the calculated one ($-880\ \mu\text{V/K}$) for n-type Si with a carrier density of $2\times10^{18}\ \text{cm}^{-3}$ at 325 K.

APPENDIX C: HEAT PARTITION MODELS

The heat partition in Table S1 [37] and the initial temperature profile T_{ini} in Fig. 3 were derived using the following equations:

(i) first atomic layer:

$$Q_0 = Q_1 + Q_2 = \rho_1 c_1 l_0 T_{\text{ini}} + \rho_2 c_2 l_0 T_{\text{ini}};$$

(ii) phonon mean free path:

$$Q_0 = Q_1 + Q_2 = \rho_1 c_1 v_1 \tau_0 T_{\text{ini}} + \rho_2 c_2 v_2 \tau_0 T_{\text{ini}};$$

(iii) thermal diffusion length:

$$Q_0 = Q_1 + Q_2 = \rho_1 c_1 \sqrt{\alpha_1 \tau_0}\ T_{\text{ini}} + \rho_2 c_2 \sqrt{\alpha_2 \tau_0}\ T_{\text{ini}};$$

(iv) half and half:

$$Q_1 = Q_0/2 = \rho_1 c_1 v_1 \tau_0 T_{\text{ini}}^1;$$

$$Q_2 = Q_0/2 = \rho_2 c_2 v_2 \tau_0 T_{\text{ini}}^2,$$

where τ_0 is the short heating time.

Using the initial temperature profile T_{ini}, we were able to obtain the evolution of the temperature profile using Green's function [65], as follows:

$$T(x,t) = \frac{1}{\sqrt{4\pi\alpha t}} \int_0^\infty (e^{-(x+y)^2/4\alpha t} + e^{-(x-y)^2/4\alpha t})T_{\text{ini}}(y)dy, \tag{C1}$$

where $T_{\text{ini}}(y)$ is the initial temperature profile. Because we assumed the square function of $T_{\text{ini}}(y)$, the integral becomes

$$\begin{aligned} T(x,t) &= \frac{T_{\text{ini}}}{\sqrt{4\pi\alpha t}} \int_0^l \left(e^{-(x+y)^2/4\alpha t} + e^{-(x-y)^2/4\alpha t}\right)dy \\ &= \frac{T_{\text{ini}}}{2}\left[\text{Erf}\left(\frac{x+l}{2\sqrt{\alpha t}}\right) - \text{Erf}\left(\frac{x-l}{2\sqrt{\alpha t}}\right)\right], \end{aligned} \tag{C2}$$

where the error function is used. When l is very small at $\tau_0 \to 0$, we obtained the following temperature profiles:

(i) first atomic layer:

$$T_{1,2}(x,t) = \frac{Q_0}{\rho_1 c_1 + \rho_2 c_2} \frac{e^{-\frac{x^2}{4\alpha_{1,2} t}}}{\sqrt{\pi \alpha_{1,2} t}}; \tag{C3}$$

(ii) phonon mean free path:

$$T_{1,2}(x,t) = \frac{Q_0 v_{1,2}}{\rho_1 c_1 v_1 + \rho_2 c_2 v_2} \frac{e^{-\frac{x^2}{4\alpha_{1,2} t}}}{\sqrt{\pi \alpha_{1,2} t}}; \tag{C4}$$

(iii) thermal diffusion length:

$$T_{1,2}(x,t) = \frac{Q_0}{\sqrt{\rho_1 c_1 k_1} + \sqrt{\rho_2 c_2 k_2}} \frac{e^{-\frac{x^2}{4\alpha_{1,2} t}}}{\sqrt{\pi t}}; \tag{C5}$$

(iv) half and half:

$$T_{1,2}(x,t) = \frac{Q_0}{2} \frac{e^{-\frac{x^2}{4\alpha_{1,2} t}}}{\sqrt{\rho_{1,2} c_{1,2} k_{1,2} \pi t}}. \tag{C6}$$

Note that the half-and-half temperature profile is completely separable and has no dependency on the sound velocity v in the final form.

APPENDIX D: NUMERICAL SOLUTIONS FOR TEMPERATURE PROFILES

Using the backward-Euler method [66], the one-dimensional heat equation in Eq. (2) was numerically solved for two semi-infinite materials in contact. Different from the explicit Euler method, the implicit method gives stable, nonoscillatory solutions for the heat equation in our numerical simulations. The system size was large enough for the propagating heat not to reach the other boundary whose temperature was kept at ambient temperature T_0. The initial heat Q_0 is injected instantaneously within 0.1 ps and propagates with a time step of 1 ps. The interfacial thermal conductance κ is fully considered to allow heat exchange at the interface.

APPENDIX E: ANALYTICAL SOLUTIONS FOR TEMPERATURE PROFILES

Because we set $\kappa = 0$, we solved Eq. (2) analytically for individual semi-infinite materials using Green's function [65], as follows:

$$T(x,t) = \int_0^s \int_0^\infty \frac{\left(e^{-\frac{(x-y)^2}{4\alpha(t-s)}} + e^{-\frac{(x-y)^2}{4\alpha(t-s)}}\right)}{\sqrt{4\pi\alpha(t-s)}} \frac{\dot{Q}(y,s)}{\rho c}\, dyds, \tag{E1}$$

with periodic heat pulses $\dot{Q}$ at the surface,

$$\dot{Q}(x,t) = \frac{1}{2} Q_0 \delta(x) \sum_{n=0}^{N} \delta(t - n\tau), \tag{E2}$$

where 1/2 comes from the heat partition postulate (see Table S1 [37]). Time t should be larger than $N\tau$. Then, the spatial and time δ-function integrations give

$$T(x,t) = \frac{Q_0}{2\rho c} \sum_{n=0}^{N} \int_0^s \frac{e^{-\frac{x^2}{4\alpha(t-s)}}}{\sqrt{4\pi\alpha(t-s)}} \delta(s - n\tau) ds \tag{E3}$$

$$= \frac{Q_0}{2\sqrt{\pi \rho c k}} \sum_{n=0}^{N} \frac{e^{-\frac{x^2}{4\alpha(t-n\tau)}}}{\sqrt{t - n\tau}}, \tag{E4}$$

which can be converted into an integral when $t \gg \tau$. In our estimation, we mostly used $t = 1$ s and $\tau = 1$ ns, satisfying the condition $t \gg \tau$. Because we know that

$$\sum_{n=0}^{N} \frac{e^{-\frac{x^2}{4\alpha(t-n\tau)}}}{\sqrt{t - n\tau}} = \int_0^{N\tau} \frac{e^{-\frac{x^2}{4\alpha(t-z)}}}{\sqrt{t - z}} \frac{dz}{\tau}, \tag{E5}$$

we derive the analytic temperature profile as

$$\begin{aligned} T(x,t) = \frac{\frac{Q_0}{\tau}}{2\sqrt{\pi\rho c k}} \Bigg[&\sqrt{t}\ \mathcal{E}_{\frac{3}{2}}\left[\frac{x^2}{4\alpha t}\right] \\ &- \sqrt{t - N\tau}\ \mathcal{E}_{\frac{3}{2}}\left[\frac{x^2}{4\alpha(t - N\tau)}\right]\Bigg], \end{aligned} \tag{E6}$$

TABLE II. Triboelectric material characteristics are listed. The material density (ρ), specific heat (c), and thermal conductivity (k) are taken from experimental results; $I\beta$-cellulose's are taken from molecular dynamics simulations. The calculated Seebeck coefficient and triboelectric factor are also displayed.

	$\boldsymbol{\rho}_{\mathbf{th}}$ (g/cm^3)	$\boldsymbol{\rho}$ (g/cm^3)	$\boldsymbol{c}$ (J/g K)	$\boldsymbol{k}$ (W/m K)	$\boldsymbol{S}$ (μV/K)	$\boldsymbol{\xi}$ (V s$^{1/2}$/J cm^{-2})
Wool [67,68]	0.82	0.026	1.37	0.034	6458	1.86
PP [69]	0.93	0.9	1.68	0.22	13821	0.239
Silk [70]	1.24	1.4	1.24	0.256	12201	0.183
Nylon [71,72]	0.95	1.24	1.50	0.27	11118	0.156
NR [73,74]	1.01	0.96	1.89	0.35	9392	0.117
Cellulose [75–77]	1.35	1.6	1.40	5.7	12604	0.035
Al [78]	2.71	2.70	0.95	238	−2.5	-1×10^{-6}
Silicon [79]	2.28	2.33	0.70	130	−1769	-1.2×10^{-3}
Quartz [78]	2.49	2.5	0.78	1.4	−13434	−0.081
Sulfur [78]	1.47	2.07	0.72	0.27	−7492	−0.118
PE [80]	0.80	0.93	1.83	0.46	−13846	−0.156
PTFE [81]	2.27	2.20	1.05	0.26	−12291	−0.158
PDMS [72]	2.25	0.97	1.6	0.2	−12568	−0.225
PVC [78]	1.44	1.38	0.96	0.15	−12449	−0.279

which consists of two terms, T_{first} and T_{second}, with different dispersion lengths and opposite polarity. The first term T_{first} is the same as Eq. (3). The second term T_{second} is negligible compared to the first term T_{first} for the condition $t \gg \tau$. $\mathcal{E}_n(x)$ is a special function called the general exponential integral, defined as

$$\mathcal{E}_m(z) = \int_1^\infty \frac{e^{-zu}}{u^m} du, \tag{E7}$$

which can be evaluated numerically.

The final solution in Eq. (3) is also valid for the continuous injection of heat at the surface with the rate of Q_0/τ, as shown in Fig. S11 [37], justifying our use of the pulse model. From the Green's function method [65] of Eq. (3), we obtain the temperature profile as

$$T(x,t) = \frac{1}{2} \frac{\frac{Q_0}{\tau}}{\rho c} \int_0^t \frac{e^{-\frac{x^2}{4\alpha(t-s)}}}{\sqrt{4\pi\alpha(t-s)}} ds \tag{E8}$$

$$= \frac{1}{2} \frac{\frac{Q_0}{\tau}}{\sqrt{\pi \rho c k}} \sqrt{t}\, \mathcal{E}_{\frac{3}{2}}\left[\frac{x^2}{4\alpha t}\right], \tag{E9}$$

which is exactly the same as Eq. (3) for $t \gg \tau$. Physically, this makes sense because both the heat generation schemes are indistinguishable for large $t \gg \tau$. Our pulse model, however, provides a richer story about the triboelectric charging process, as we discussed in the main text. Also, our stationary heat generator model at the interface for static electrification is applicable not only for frictional heat, but also for other heat sources such as interfacial chemical reactions, artificial heaters, and laser pulses.

APPENDIX F: SURFACE CHARGE DENSITY

With the information of ε and S, the charge density distribution can be obtained from the second derivative of the temperature profile as $\rho_e = \varepsilon S \nabla^2 T$. Because no charge escaped from the semi-infinite material, the net charge should always be zero, as $\int_0^\infty \rho_e dx = 0$. As Eq. (E6) consists of two terms, T_{first} and T_{second}, the integral of the charge density distribution also consists of two terms, σ_{first} and σ_{second}, which are equal in magnitude but opposite in sign. σ_{first} corresponds to the inner charge because its distribution is very wide with the dispersion length of $2\sqrt{\alpha t}$. On the other hand, σ_{second} is very localized at the interface with the $2\sqrt{\alpha(t - N\tau)}$ dispersion, thus corresponding to the δ-function-like surface-charge density, σ_{surface}. Then, σ_{surface} was obtained by integrating $\varepsilon S \nabla^2 T_{\text{second}}$ as

$$\sigma_{\text{surface}} = \int_0^\infty \varepsilon S \nabla^2 T_{\text{second}}(x,t) dx, \tag{F1}$$

which results in Eq. (4), which is independent of time t.

APPENDIX G: TRIBOELECTRIC MATERIAL CHARACTERISTICS

See Table II for the triboelectric material characteristics.

APPENDIX H: SIMILARITY OF TRIBOELECTRIC SERIES

To compare the two triboelectric series, we define a similarity function of $s(M_i, M_j) = 1$ if the triboelectric order for M_i and M_j materials in a series is the same with respect to the reference series, and $s(M_i, M_j) = 0$ if the order is different. We chose our quantitative triboelectric series as the reference. Average $\bar{s}$ was calculated for all possible combinations. If two series had the same order, then $\bar{s} = 1$. If two series were random, then $\bar{s} = 0.5$. If two series were completely opposite, $\bar{s} = 0$. Averaged value of $\bar{s}$ for five experimental series with reference to the quantitative series was about 0.83.

[1] P. E. Shaw, The electrical charges from like solids, Nature (London) **118**, 659 (1926).

[2] L. B. Loeb, The basic mechanisms of static electrification, Science **102**, 573 (1945).

[3] D. K. Davies, Charge generation on dielectric surfaces, J. Phys. D: Appl. Phys. **2**, 307 (1969).

[4] C. F. Gallo and W. L. Lama, Some charge exchange phenomena explained by a classical model of the work function, J. Electrostat. **2**, 145 (1976).

[5] J. Lowell and A. C. Rose-Innes, Contact electrification, Adv. Phys. **29**, 947 (1980).

[6] R. G. Horn, D. T. Smith, and A. Grabbe, Contact electrification induced by monolayer modification of a surface and relation to acid-base interactions, Nature (London) **366**, 442 (1993).

[7] H. T. Baytekin, A. Z. Patashinski, M. Branicki, B. Baytekin, S. Soh, and B. A. Grzybowski, The mosaic of surface charge in contact electrification, Science **333**, 308 (2011).

[8] C. Xu, A. C. Wang, H. Zou, B. Zhang, C. Zhang, Y. Zi, L. Pan, P. Wang, P. Feng, Z. Lin, and Z. L. Wang, Raising the working temperature of a triboelectric nanogenerator by quenching down electron thermionic emission in contact-electrification, Adv. Mater. **30**, 1803968 (2018).

[9] Y. Wang, N. Yamada, J. Xu, J. Zhang, Q. Chen, Y. Ootani, Y. Higuchi, N. Ozawa, M.-I. D. B. Bouchet, J. M. Martin, S. Mori, K. Adachi, and M. Kubo, Triboemission of hydrocarbon molecules from diamond-like carbon friction interface induces atomic-scale wear, Sci. Adv. **5**, eaax9301 (2019).

[10] C. A. Mizzi, A. Y. W. Lin, and L. D. Marks, Does Flexoelectricity Drive Triboelectricity?, Phys. Rev. Lett. **123**, 116103 (2019).

[11] H. Zou, Y. Zhang, L. Guo, P. Wang, X. He, G. Dai, H. Zheng, C. Chen, A. C. Wang, C. Xu, and Z. L. Wang, Quantifying the triboelectric series, Nat. Commun. **10**, 1427 (2019).

[12] H. Zou, L. Guo, H. Xue, Y. Zhang, X. Shen, X. Liu, P. Wang, X. He, G. Dai, P. Jiang, H. Zheng, B. Zhang, C. Xu, and Z. L. Wang, Quantifying and understanding the triboelectric series of inorganic non-metallic materials, Nat. Commun. **11**, 2093 (2020).

[13] D. J. Lacks and T. Shinbrot, Long-standing and unresolved issues in triboelectric charging, Nat. Rev. Chem. **3**, 465 (2019).

[14] S. Lin, L. Xu, A. Chi Wang, and Z. L. Wang, Quantifying electron-transfer in liquid-solid contact electrification and the formation of electric double-layer, Nat. Commun. **11**, 399 (2020).

[15] T. R. Ducati, L. H. Simões, and F. Galembeck, Charge partitioning at gas-solid interfaces: Humidity causes electricity buildup on metals, Langmuir **26**, 13763 (2010).

[16] J. Nie, Z. Wang, Z. Ren, S. Li, X. Chen, and Z. L. Wang, Power generation from the interaction of a liquid droplet and a liquid membrane, Nat. Commun. **10**, 2264 (2019).

[17] E. R. Williams, The electrification of thunderstorms, Sci. Am. **259**, 88 (1988).

[18] S. Pan and Z. Zhang, Fundamental theories and basic principles of triboelectric effect: A review, Friction **7**, 2 (2019).

[19] D. J. Lacks, The unpredictability of electrostatic charging, Angew. Chem. Int. Ed. **51**, 6822 (2012).

[20] T. Noh *et al.*, *Science 2* (Chunjae Education, Seoul, 2015), p. 48, http://textbook.chunjae.co.kr/textbook/textbook_gallery2015.aspx?mode =v&ClassA=A6-C2-NN-NN-04-04-0-0-0-0-0-0.

[21] J. Lowell and W. S. Truscott, Triboelectrification of identical insulators. II. Theory and further experiments, J. Phys. D: Appl. Phys. **19**, 1281 (1986).

[22] T. Shinbrot, T. S. Komatsu, and Q. Zhao, Spontaneous tribocharging of similar materials, Europhys. Lett. **83**, 24004 (2008).

[23] M. M. Apodaca, P. J. Wesson, K. J. M. Bishop, M. A. Ratner, and B. A. Grzybowski, Contact electrification between identical materials, Angew. Chem. Int. Ed. **49**, 946 (2010).

[24] D. J. Lacks and A. Levandovsky, Effect of particle size distribution on the polarity of triboelectric charging in granular insulator systems, J. Electrostat. **65**, 107 (2007).

[25] V. Lee, S. R. Waitukaitis, M. Z. Miskin, and H. M. Jaeger, Direct observation of particle interactions and clustering in charged granular streams, Nat. Phys. **11**, 733 (2015).

[26] L. S. McCarty and G. M. Whitesides, Electrostatic charging due to separation of ions at interfaces: Contact electrification of ionic electrets, Angew. Chem. Int. Ed. **47**, 2188 (2008).

[27] N. Gibson, Static electricity—an industrial hazard under control? J. Electrostat. **40–41**, 21 (1997).

[28] H.-K. Lyeo and D. G. Cahill, Thermal conductance of interfaces between highly dissimilar materials, Phys. Rev. B **73**, 144301 (2006).

[29] P. S. H. Henry, The role of asymmetric rubbing in the generation of static electricity, Braz. J. Appl. Phys. **4**, S31 (1953).

[30] W. R. Harper, Contact electrification of semiconductors, Braz. J. Appl. Phys. **11**, 324 (1960).

[31] E.-S. Lee, S. Cho, H.-K. Lyeo, and Y.-H. Kim, Seebeck Effect at the Atomic Scale, Phys. Rev. Lett. **112**, 136601 (2014).

[32] H. Kim, Y. H. Chang, W.-J. Jang, E.-S. Lee, Y.-H. Kim, and S.-J. Kahng, Probing single-molecule dissociations from a bimolecular complex NO–Co-porphyrin, ACS Nano **9**, 7722 (2015).

[33] G. Zilibotti, S. Corni, and M. C. Righi, Load-Induced Confinement Activates Diamond Lubrication by Water, Phys. Rev. Lett. **111**, 146101 (2013).

[34] S. Kajita and M. C. Righi, A fundamental mechanism for carbon-film lubricity identified by means of *ab initio* molecular dynamics, Carbon **103**, 193 (2016).

[35] N. W. Ashcroft and N. D. Mermin, *Solid State Physics* (Cengage Learning, Boston, 1976).

[36] S. Cho, S. D. Kang, W. Kim, E.-S. Lee, S.-J. Woo, K.-J. Kong, I. Kim, H.-D. Kim, T. Zhang, J. A. Stroscio, Y.-H. Kim, and H.-K. Lyeo, Thermoelectric imaging of structural disorder in epitaxial graphene, Nat. Mater. **12**, 913 (2013).

[37] See Supplemental Material at http://link.aps.org/supplemental/10.1103/PhysRevResearch.4.023131 for schematic diagrams, numerical solutions, additional temperature profiles, van der Waals contacts, atomic models, and additional tables for heat partition, van der Waals interaction, dielectric constants, and HSE06 mixing parameters.

[38] A. D. Avery, B. H. Zhou, J. Lee, E.-S. Lee, E. M. Miller, R. Ihly, D. Wesenberg, K. S. Mistry, S. L. Guillot, B. L. Zink, Y.-H. Kim, J. L. Blackburn, and A. J. Ferguson, Tailored semiconducting carbon nanotube networks with enhanced thermoelectric properties, Nat. Energy **1**, 16033 (2016).

[39] C. G. Van de Walle and J. Neugebauer, Universal alignment of hydrogen levels in semiconductors, insulators and solutions, Nature (London) **423**, 626 (2003).

[40] C.-S. Liu, G. Pilania, C. Wang, and R. Ramprasad, How critical are the van der Waals interactions in polymer crystals?, J. Phys. Chem. A **116**, 9347 (2012).

[41] G. Natta and P. Corradini, Structure and properties of isotactic polypropylene, Nuovo. Cim. **15**, 40 (1960).

[42] Y. Takahashi and T. Kumano, Crystal structure of natural rubber, Macromolecules **37**, 4860 (2004).

[43] S. Sharma and A. Kumar, *Keratin as a Protein Biopolymer* (Springer, Cham, 2019).

[44] A. Y. Feldman, M. Fernanda Gonzalez, E. Wachtel, M. P. Moret, and G. Marom, Transcrystallinity in aramid and carbon fiber reinforced nylon 66: Determining the lamellar orientation by synchrotron X-ray micro diffraction, Polymer **45**, 7239 (2004).

[45] J. O. Warwicker, The crystal structure of silk fibroin, Acta Cryst. **7**, 565 (1954).

[46] Y. Nishiyama, P. Langan, and H. Chanzy, Crystal structure and hydrogen-bonding system in cellulose Iβ from synchrotron X-ray and neutron fiber diffraction, J. Am. Chem. Soc. **124**, 9074 (2002).

[47] M. Tosaka and K. Tashiro, Crystal polymorphism and structure models of poly(dimethylsiloxane), Polymer **153**, 507 (2018).

[48] A. Moyassari, M. Unge, M. S. Hedenqvist, U. W. Gedde, and F. Nilsson, First-principle simulations of electronic structure in semicrystalline polyethylene, J. Chem. Phys. **146**, 204901 (2017).

[49] H. Blok, The flash temperature concept, Wear **6**, 483 (1963).

[50] G. Kleyman, T. Kang, J. Twiefel, and W. Voit, Characterization of triboelectric charge generation between PTFE and nylon after repeated contacts, Energy Harvest. Syst. **4**, 165 (2018).

[51] S. P. Hersh and D. J. Montgomery, Static electrification of filaments, Text. Res. J. **25**, 279 (1955).

[52] J. Henniker, Triboelectricity in polymers, Nature (London) **196**, 474 (1962).

[53] K. A. Charles, *Nature's Electricity* (McGraw-Hill, New York, 1987).

[54] N. Jonassen, *Electrostatics* (Springer, Boston, 1998).

[55] S. A. Putnam, D. G. Cahill, and G. C. L. Wong, Temperature dependence of thermodiffusion in aqueous suspensions of charged nanoparticles, Langmuir **23**, 9221 (2007).

[56] K. Kadoya, N. Matsunaga, and A. Nagashima, Viscosity and thermal conductivity of dry air in the gaseous phase, J. Phys. Chem. Ref. Data **14**, 947 (1985).

[57] Y. Liu, Y. Huang, and X. Duan, van der Waals integration before and beyond two-dimensional materials, Nature (London) **567**, 323 (2019).

[58] G. Kresse and D. Joubert, From ultrasoft pseudopotentials to the projector augmented-wave method, Phys. Rev. B **59**, 1758 (1999).

[59] J. P. Perdew, K. Burke, and M. Ernzerhof, Generalized Gradient Approximation Made Simple, Phys. Rev. Lett. **77**, 3865 (1996).

[60] A. V. Krukau, O. A. Vydrov, A. F. Izmaylov, and G. E. Scuseria, Influence of the exchange screening parameter on the performance of screened hybrid functionals, J. Chem. Phys. **125**, 224106 (2006).

[61] M. A. L. Marques, J. Vidal, M. J. T. Oliveira, L. Reining, and S. Botti, Density-based mixing parameter for hybrid functionals, Phys. Rev. B **83**, 035119 (2011).

[62] Y. Kang, S. H. Jeon, Y. Cho, and S. Han, *Ab initio* calculation of ionization potential and electron affinity in solid-state organic semiconductors, Phys. Rev. B **93**, 035131 (2016).

[63] S. Kasap, *Thermoelectric Effects in Metals: Thermocouples* (an e-booklet, 2001), http://courses.nus.edu.sg/course/elengv/ee3406/seebeck and thermocouple.pdf.

[64] A. Stranz, J. Kähler, A. Waag, and E. Peiner, Thermoelectric properties of high-doped silicon from room temperature to 900 K, J. Electron. Mater. **42**, 2381 (2013).

[65] J. R. Cannon and F. E. Browder, *The One-Dimensional Heat Equation* (Cambridge University Press, Cambridge, 1984).

[66] J. C. Butcher, *Numerical Methods for Ordinary Differential Equations* (Wiley, New Jersey, 2016).

[67] A. R. Haly, I. Abu-Isa, and M. Dole, Specific heat of wool in the temperature range -50 to 100 °C, J. Appl. Polym. Sci. **9**, 893 (1965).

[68] Z. Ye, C. M. Wells, C. G. Carrington, and N. J. Hewitt, Thermal conductivity of wool and wool-hemp insulation, Int. J. Energy Res. **30**, 37 (2006).

[69] D. Tripathi, *Practical Guide to Polypropylene* (iSmithers Rapra, Shrewsbury, 2002).

[70] J. Yong, B. Hassan, Y. Liang, K. Ganesan, R. Rajasekharan, R. Evans, G. Egan, O. Kavehei, J. Li, G. Chana, B. Nasr, and E. Skafidas, A silk fibroin bio-transient solution processable memristor, Sci. Rep. **7**, 14731 (2017).

[71] K. Xie, Y. He, J. Cai, and W. Hu, Thermal conductivity of Nylon 46, Nylon 66 and Nylon 610 characterized by flash DSC measurement, Thermochim. Acta **683**, 178445 (2020).

[72] J. E. Mark, *Physical Properties of Polymers Handbook* (Springer, New York, 2007).

[73] Y. He, L.-X. Ma, Y.-Z. Tang, Z.-P. Wang, W. Li, and D. Kukulka, Thermal conductivity of natural rubber using molecular dynamics simulation, J. Nanosci. Nanotechnol. **15**, 3244 (2015).

[74] R. W. Warfield and M. C. Petree, Thermodynamic properties of natural rubber and isoprene, Rubber Chem. Technol. **39**, 143 (1966).

[75] K. Mazeau and L. Heux, Molecular dynamics simulations of bulk native crystalline and amorphous structures of cellulose, J. Phys. Chem. B **107**, 2394 (2003).

[76] J. A. Diaz, Z. Ye, X. Wu, A. L. Moore, R. J. Moon, A. Martini, D. J. Boday, and J. P. Youngblood, Thermal conductivity in nanostructured films: From single cellulose nanocrystals to bulk films, Biomacromolecules **15**, 4096 (2014).

[77] Engineering ToolBox, *Specific Heat of Some Common Substances*, https://www.engineeringtoolbox.com/specific-heat-capacity-d_391.html.

[78] *Thermophysical Properties of Materials for Nuclear Engineering: A Tutorial and Collection of Data* (International Atomic Energy Agency, Vienna, 2009).

[79] H. R. Shanks, P. D. Maycock, P. H. Sidles, and G. C. Danielson, Thermal conductivity of silicon from 300 to 1400 °K, Phys. Rev. **130**, 1743 (1963).

[80] Y. Jannot and P. Meukam, Simplified estimation method for the determination of the thermal effusivity and thermal conductivity using a low cost hot strip, Meas. Sci. Technol. **15**, 1932 (2004).

[81] J. Blumm, A. Lindemann, M. Meyer, and C. Strasser, Characterization of PTFE using advanced thermal analysis techniques, Int. J. Thermophys. **31**, 1919 (2010).